Journal of Engineering Science and Technology
Vol. 18, No. 1 (2023) 693 - 705

NUMERICAL THERMAL ANALYSIS OF RE-ENTRY APOLLO MODEL AS-202 AT HIGH ANGLE OF ATTACK

FARHAN L. RASHID[1], EMAD Q. HUSSEIN[1],
LAITH J. HABEEB[2], AHMED KADHIM HUSSEIN[3],
MOHAMED BECHIR BEN HAMIDA[4,5,6], BAGH ALI[7], OBAI YOUNIS[8,*]

[1]Department of Petroleum Engineering, College of Engineering,
University of Kerbala, Karbala, Iraq
[2]Mechanical Engineering Department, Faculty of Engineering,
University of Technology, Baghdad, Iraq
[3]Mechanical Engineering Department, College of Engineering,
University of Babylon, Babylon City, Iraq
[4]College of Engineering, Department of Mechanical Engineering,
Imam Mohammad Ibn Saud Islamic University (IMSIU), Riyadh, Saudi Arabia
[5]Research Laboratory of Ionized Backgrounds and Reagents Studies (EMIR),
Preparatory Institute for Engineering Studies of Monastir (IPEIM),
University of Monastir, Monastir City, Tunisia
[6]Higher School of Sciences and Technology of Hammam Sousse (ESSTHS),
Department of Physics, University of Sousse, Tunisia
[7]Faculty of Computer Science and Information Technology,
Superior University, Lahore 54000, Pakistan
[8]Department of Mechanical Engineering, College of Engineering in Wadi
Addwasir, Prince Sattam Bin Abdulaziz University, Al-kharj 11942 , KSA
*Corresponding author: o.elamin@psau.edu.sa

Abstract

Re-entry Apollo model AS-202 became a popular research area in the aerospace industries recognized the importance of the field for various interests' applications owing to its capability to resist the high heating loads through the re-entry stage. This work employs Computational Fluid Dynamics (CFD) to analyse the heat transfer and thermal stresses of a capsule entering the atmosphere of Earth at free-stream Mach No. 6 and 10. The coupled, nonlinear partial differential equations that describe the physical phenomenon are solved using the 3D finite element method to predict the pressure and temperature distribution over the Apollo at different attack angles. Subsequently, the resulting stress and deformation occurring on Apollo have been obtained. The dynamic mesh and user-defined function are applied to control the position of Apollo at the setting Angle of Attack (AoA). The result depicted extreme temperature at the heat shield and decreased potential and kinetic energy. The pressure over the after body stays nearly constant, reflecting a separated flow at the base. The equivalent stress-induced and the total deformation corresponding to the flow have been successfully computed. Based on the results presented, the equivalent stress increases with increasing the angle of attack, while the deformation decreases with the attack angle. The predicted aerodynamic characteristic of the 3D Apollo has been successfully compared with the previous measurement.

Keywords: Aerodynamic characteristics, Angle of attack, Apollo Mission AS-202, Thermal Analysis.

1. Introduction

An understanding of heat transfer and fluid flow in porous media is important in many engineering fields, such as soil mechanics, powder metallurgy, chemical processing, and petroleum reservoir recovery [1]. During the conceptual design stage of re-entry vehicles, the design parameters are varied to gain knowledge of their effect on the vehicle's overall performance and its capability to fulfil the design requirements. One of the defining characteristics of an entry vehicle is its shape, as this shape will largely define the aerothermodynamics characteristics of the vehicle. Since aerothermodynamics challenges, such as vehicle heating, remain one of the most difficult problems in atmospheric re-entry, an exploration of the possible shapes of a vehicle early in the design is advisable [2].

To obtain thermal stresses in critical components limiting the maximum allowable heating rates, it is essential to find the heat transfer coefficient and fluid temperature on the internal pressure components surface [3]. Lacking an accurate method to measure the transient temperature of the fluid drives to determine thermal stresses by solving the inverse heat conduction problem. The entire element transient temperature distribution is obtained based on the wall transient temperature measured at the outer easily reachable surface of the pressure component. Then thermal stresses are determined [4].

Flying faster and higher are the primary goals dominantly driving aerospace science development and enhancements. Recent applications of hypersonic flight are primarily related to space flight movements, although it extends to passenger transportation to some extent. The heat flux and base pressure are of principal importance for the efficient evolution of parachutes and successful spacecraft landing [5]. The bow shock wave is made ahead of the blunt body, surrounded by a subsonic-supersonic region between the bow shock wave and the blunt body. Chester and Freeman analysed the location of the sonic line, wall pressure distribution analytically, and shock stand-off distance on the region of the spherical cap at different high speeds and an adiabatic index near unity envisaging a singular point at an angle of 60° from the stagnation point. However, the high-speed analytical model over the blunt body is concluded to be sophisticated and the most complex [6]. These hypersonic flight situations are coupled with many complex aerodynamic problems.

Consequently, the successful staffed entries of the Apollo, Gemini, and Mercury vehicles led to hypersonic research success [7-10]. CFD is an economic approximation to present these flows. It's utilized to run sophisticated hypersonic effects. A significant part of the atmospheric re-entry vehicle design is thermal analysis since they are exposed to intense aerodynamic heating. Koike et al. [11] used a numerical approach to simulate the aerodynamic heating around a flare-type membrane vehicle through the Earth's atmospheric re-entry. The approach results evinced that the distribution of heat flux varies with the raise in attack angle because of the changes in heat flux, and the flow field at the stagnation point for an attack angle of 40 degrees was 3.09 greater than that for 0 degrees.

Hussein et al. [12, 13] presented the temperature distribution and aerodynamic heating in the conical nose and an ogive of a fly body using dynamic mesh. The results showed that the temperature distribution and internal heat surrounding the body nose are directly proportional to the Angle of Attack (AoA) and Mach number. Wang and Elgohary [14] employed a new approach to design the

atmospheric entry of the Mars capsule controller using networks of Apollo entry data and deep neutral for flight-proven. The controller has been used to module the angle of the bank with available data from the simulations of the Apollo entry. In comparison to the Apollo controller, the current technique achieves the same degree of precision for both nonlinear and linear entry dynamics.

Schouler et al. [15] gathered data from a range of space missions from the flight and ground wind tunnels in a rarefied atmosphere, as well as their numerical reconstruction. de Wit et al. [16] suggested the use of a multi-level optimization (MLO) method for aircraft rubber design based on analytical target cascading (ATC). Khanna and Kotousov [17] examined the present state-of-the-art contemporary computational techniques that may assist aircraft Full-Scale Fatigue Tests (FSFTs).

It is essential to understand the actual physical phenomena of Re-entry Apollo to predict thermal loads through the re-entry stage with varied angles of attack, as shown in Fig. 1 [3].

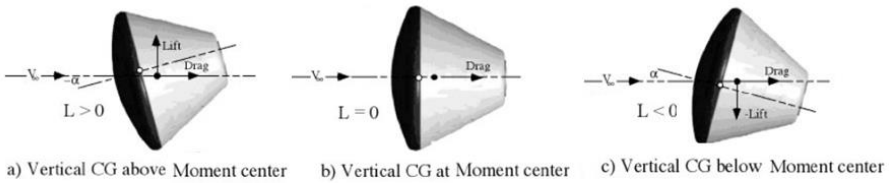

Fig. 1. Apollo with different angles of attack.

Hypersonic test features for experimental work are exceptionally expensive and not feasible, which signifies the necessity of using CFD as an alternative to provide high-fidelity solutions and an in-depth understanding of the thermal flow characteristics around and within the material of the Apollo vehicle. Therefore, this study aims to provide efficient engineering procedures for estimating the pressure and temperature over the surface of the Re-entry Apollo Model AS-202 geometry at different attack angles using the CFD tools. The model employs the dynamic mesh technique to simulate the change in the attack angle using a user-defined function (UDF). After the simulation, we can observe the velocity and pressure contours over the surface of Apollo, and we can also examine the stresses and displacements created in the Apollo wall due to the effect of pressure and temperature at various angles of attack. This knowledge will assist researchers and material engineers in using composite materials for aerospace automotive.

2. Aerodynamic Heating

During the re-entry phase operation of the atmospheric re-entry vehicles, a process called aerodynamic heating is generated. This process can be defined as solid-body heating created via the fluid transit over the body. It's a type of forced heat convection in which the forces after those related to the thermal processes create the flow field. Aerodynamic heating produces heat, and thus all outer vehicle surfaces are heated. Thermal protection systems are needed to keep the internal vehicle structure from the high fluxes of heat on the outer surfaces. The design principle of the thermal protection system is that the energy emitted by the

aerodynamic heating should be rejected or absorbed via the systems of thermal protection. Figure 2 reveals the three dimensions of the Apollo model AS-202.

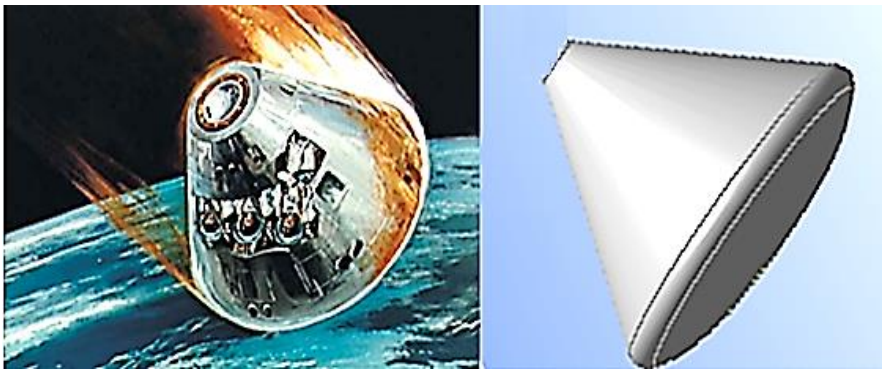

Fig. 2. Apollo model AS-202 in 3D [19].

3.Methodology

The analysis of CFD on a re-entry vehicle was carried out through four procedures: (1) generating a suitable geometry of the re-entry vehicle in computer software, (2) importing this geometry into the analysis, (3) meshing the geometry in CFD software and applying the boundary conditions, (4) processing the output and assessing the results. The heating environment of the after body for the Apollo AS-202 Command Module was used as a basis to compare the CFD results with flight data. The outer module line of the AS-202, as developed for the CFD analysis, is illustrated in Fig. 3. The angle of the small side slip was ignored in the present simulations.

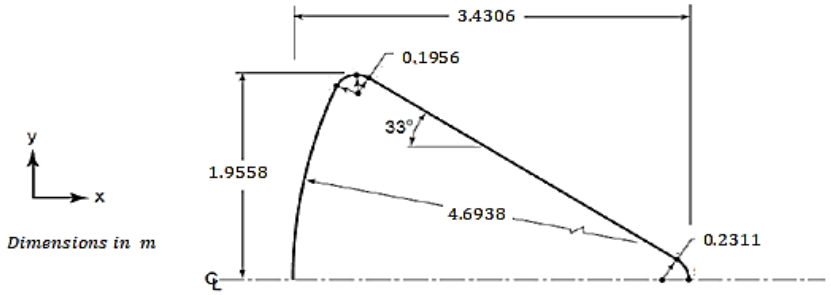

Fig. 3. Schematic representation of Apollo model AS-202 [19].

3.1. Modeling of the geometry

The Apollo As-202 Module included the fore-body of the spherical section and a 330 conical after-body. The module is a cone of 330 half-angle with the blunt shaped from a spherical segment having a radius of 4.694 m. A toroidal section having a radius of 0.196 m makes a transition between spherical and conical sections. The maximum capsule's diameter is 3.91 m, which is located in the toroidal section. The area around the re-entry model vehicle is meshed instead of the re-entry vehicle itself. The mechanical and thermal properties of the materials

used are reported in Tab. 1. The trajectory points and free stream conditions are presented in Tab. 2.

Table 1. Thermal and mechanical properties for the materials used [17].

AL-alloy	Thermal conductivity, k	160 W/m.K
	Density, ρ	2270 kg/m^3
	Thermal expansion, α	2.3×10^{-5} 1/^{o}C
	Elastic young's modulus, E	71×10^9 N/m^2
	Poisson's ratio, ν	0.33
Stainless steel	Thermal conductivity, k	15.1 W/m.K
	Density, ρ	7750 kg/m^3
	Thermal expansion, α	1.7×10^{-5} 1/^{o}C
	Elastic young's modulus, E	193×10^9 N/m^2
	Poisson's ratio, ν	0.31
Insulation	Thermal conductivity, k	0.3 W/m.K
	Density, ρ	0.05 kg/m^3
	Specific heat, cp	440 J/kg.K
AL-honeycomb	Thermal conductivity, k	237 W/m.K
	Density, ρ	2700 kg/m^3
	Thermal expansion, α	23.1×10^{-5} 1/^{o}C
	Elastic young's modulus, E	70×10^9 N/m^2
	Poisson's ratio, ν	0.35

Table 2. Conditions of free stream and trajectory points [18].

Altitude (km)	Mach No.	Pressure N/m^2	Temperature (K)	Density (kg/m^3)	Viscosity (N.s/m^2)
15	6	1.204×10^{-4}	216.65	0.193	1.4322×10^{-5}
35	10	5.589×10^{-2}	237.0	0.00821	1.5455×10^{-5}

3.2. CFD modeling

The 3D CFD simulation of re-entry vehicle thermal characteristics was developed using ANSYS Fluent. It includes solutions of continuity momentum and energy equations. The continuity equation is represented as [19, 20]:

$$\frac{\partial \rho}{\partial t} + \nabla.(\rho v) = 0 \quad (1)$$

The momentum equation can be written as:

$$\frac{\partial \rho}{\partial t} + (\rho v) + \nabla.(\rho v v) = -\nabla P + \nabla.(\bar{\tau}) + \rho g + F \quad (2)$$

The term stress tensor is written as;

$$\tau = \mu(\nabla v + \nabla v^T) - \frac{2}{3}\nabla.vI) \quad (3)$$

where I denote the unit tensor.

The energy equation is represented as:

$$\rho C_p(\frac{\partial T}{\partial t} + v_x\frac{\partial T}{\partial t} + v_y\frac{\partial T}{\partial t}) = \lambda\left(\frac{\partial^2 T}{\partial x^2} + \frac{\partial^2 T}{\partial y^2}\right) \quad (4)$$

The turbulent kinetic energy (k) and the rate of specific dissipation (ω) can be obtained from the equations:

$$\frac{\partial}{\partial t}(\rho k) + \frac{\partial}{\partial x}(\rho k v_x) + \frac{\partial}{\partial y}(\rho k v_y) = \frac{\partial}{\partial x}\left(\Gamma_k\frac{\partial \lambda}{\partial t}\right) + \frac{\partial}{\partial y}\left(\Gamma_k\frac{\partial \lambda}{\partial t}\right) + G_k - Y_k + S_k \quad (5)$$

$$\frac{\partial}{\partial t}(\rho\omega)+\frac{\partial}{\partial x}(\rho\omega v_x)+\frac{\partial}{\partial y}(\rho\omega v_y)=\frac{\partial}{\partial x}\left(\Gamma_\omega\frac{\partial k}{\partial t}\right)+\frac{\partial}{\partial y}\left(\Gamma_\omega\frac{\partial k}{\partial t}\right)+G_\omega-Y_\omega+S_\omega \quad (6)$$

The effective diffusivities for the *k*-ωmodel can be expressed as

$$\left.\begin{aligned}\Gamma_k&=\mu+\frac{\mu_1}{\sigma_k}\\ \Gamma_\omega&=\mu+\frac{\mu_1}{\sigma_\omega}\end{aligned}\right\} \quad (7)$$

where the terms Y_k, G_k denote the turbulence kinetic energy production dissipation, G_ω , Y_ω denote the specific dissipation rate production and dissipation and μ_1 denotes the turbulent viscosity.

3.3. Boundary conditions

The quality of the computational domain plays an important role in the calculation accuracy and stability. For an external flow such as that over an Apollo model AS-202, a far-field boundary should be defined, and the region between the Apollo geometry and boundary needs to be meshed. After completing the geometry meshing, boundary conditions were applied to execute the model. The Density-based approach was applied as it is preferred in high-speed compressible fluid flows. ANSYS Fluent was employed as a base solver to solve the compressible fluid flow's 3-D Reynolds Averaged Nervier Stokes equation. The system's operating pressure was set using Tab. 2, which is equal to the absolute pressure as the gauge pressure on the outlet was set to zero. In Fluent, the pressure-based solver is used in the coupled algorithm. However, the pressure-based continuity and momentum equations are solved simultaneously in each iteration, while the other equations are updated separately.

3.4. Dynamic mesh

The new dynamic mesh technique is applied in transient simulation to sustain a high mesh quality by preventing the formation of the negative cell volumes generated from the deterioration of the mesh quality. The demands of a dynamic simulation are a boundary motion description and an initial mesh which is illustrated in Fig. 4. The grid independence study can be carried out by increasing the number of elements until the value of the coefficient of pressure reaches a constant value, the mesh is refined and reaches a constant parameter of the pressure coefficient. This paper describes the attack angle by using a UDF. The UDF describes the motion of the mesh through the dynamic zone. The moving wall motion is described using the UDF code.

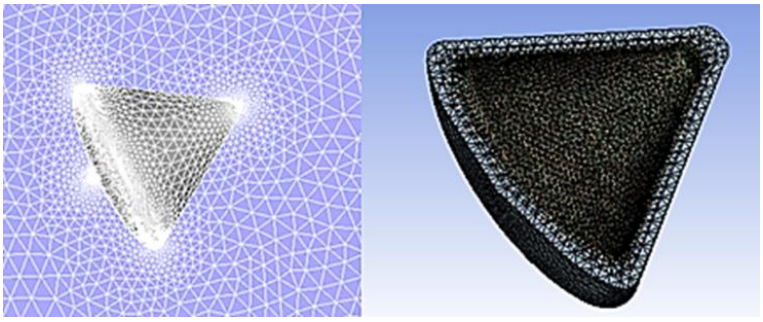

Fig. 4. Mesh generation of the Apollo.

4. Results and Discussion

The 3D simulation was conducted employing Fluent software at variable angles of attack, pressure, and temperature over the surface of Apollo under a high supersonic fluid flow. The altitude effect and variation of properties with the height were considered at the free stream conditions [21]; all results at the altitude air pressure, air temperature and viscosity are presented in Tab 2. To validate the simulation accuracy of the model, the CFD results were compared with a wind tunnel test in the literature [21]. The same parameters of structure design were used to develop the simulation model. Also, the same operating conditions were used to predict the lift coefficient and drag coefficient in the range of attack angle variation at Mach No.5 and Reynolds number equal 7×10^5. Both results are plotted in Figs. 5 and 6 and manifest that the CFD prediction is close to the experimental results. The maximum percentage difference in aerodynamic characteristics in the range of attack angle variations is less than 12%whichsatisfies the requirement of engineering accuracy. The error is mostly related to the treatment of boundary layers.

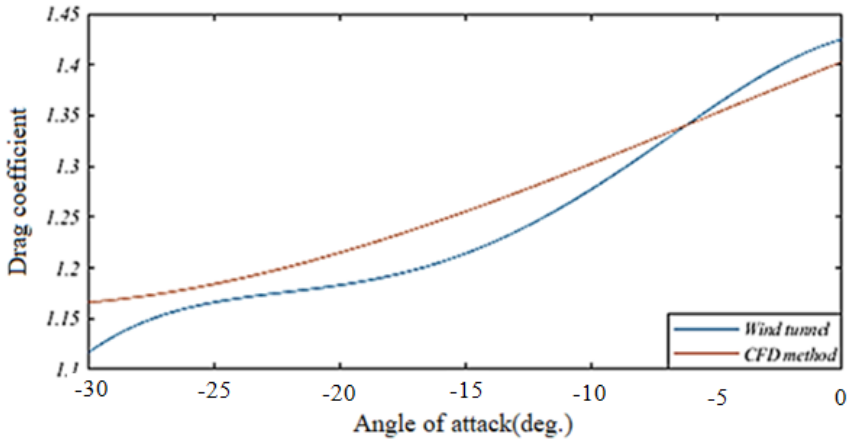

Fig. 5. Drag coefficient with varies the angle of attack at Mach 5 and Re= 7×10^{-5}.

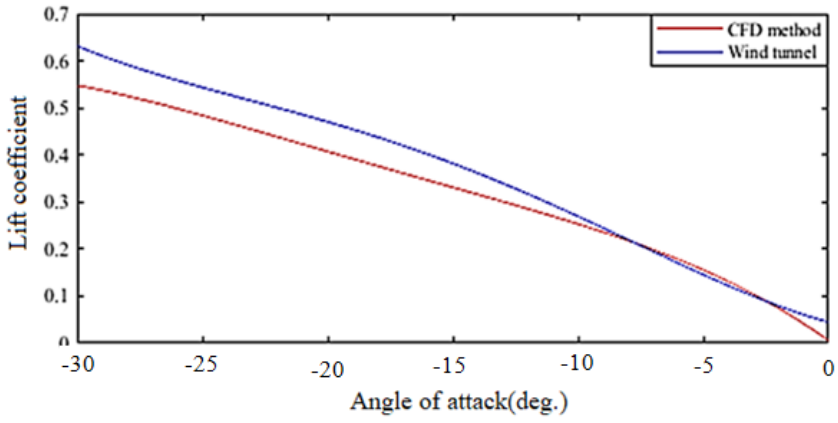

Fig.6. Lift coefficient with varies the angle of attack at Mach 5 and Re= 7×10^{-5}.

The temperature contours over the Apollo capsule, as shown in Fig. 7, at Mach number equals 10, and the angle of attack equals -30 degrees. It shows a significant increase in the temperature at the heated shield, whereas the kinetic and potential energy is reduced. Here, the potential and kinetic energy are reduced and dispersed in the form of heat energy. Thus, an isolated total energy system remains constant depending on the conservation law. It was found that the magnitude of extreme temperature at the fore-body region was 4.831×10^3 K, whereas the maximum temperature is at the re-entry vehicle's base. Figure 8 manifests the temperature distribution in the thickness of the Apollo. It was noticed that the temperature decreases with the thickness of Apollo because the insulation material reduces the energy transfer from the outer surface to the inner. Figure 9 elucidates the temperature graph concerning the angle of attack, and the temperature starts to increase as the angle of attack increases and then decreases at -15 degrees. The temperature starts to increase later, reaching a peak value of 1000 K at an attack angle of 30 degrees. The field of flow over the body of Apollo is initialized to the free-stream values in the present work. As the simulation advances, the boundary layer and the bow shock on the vehicle are created, resulting in the flow separation after the body, where the shape of the separation bubbles occurs upon the windward side. A big re-circulation bubble is developed upon the leeward side, and the shear layer that encloses the separation bubble coalesces at the neck. When the re-entry vehicle enters the atmosphere, the recompression shock is formed, and the bow shock is generated at the vehicle base.

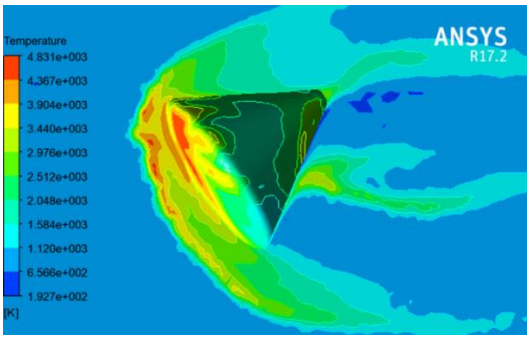

Fig. 7. Variation of temperature contour for the Apollo at Mach 10 and AoA=-30°.

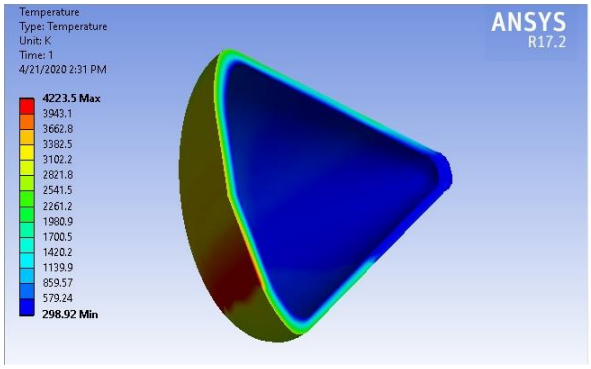

Fig. 8. Temperature distribution over the thickness of the Apollo model at Mach 10 and AoA=-30°.

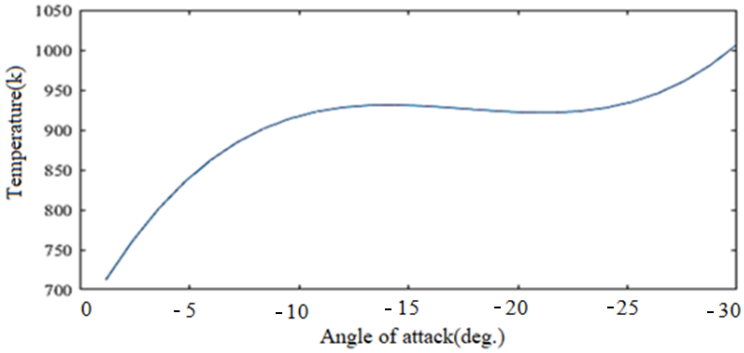

Fig. 9. Temperature distribution at Mach 6 and different values of attack angle.

The contour of pressure distributed over the Apollo model As-202 at a Mach No. of 10 and attack angle equal to -30 degrees is revealed in Fig. 10. It is shown that the fore-body exhibits the highest pressure value of 1.42×10^5 Pa, while the minimum pressure value is -5.53×10^2 Pa. It is found that the high-pressure regions appear at the leading edge and on the lower surface of Apollo, while the low-pressure region appears on the upper surface of the Apollo. Due to the strong bow shock created in the far field of the re-entry vehicle, the drag force that acts upon the vehicle increases, and Mach numbers decrease. The predicted pressure on the Apollo section, in general, agreed with the wind tunnel test.

The model's pressure was also calculated, as shown in Fig. 11, for a Mach number of 6 and different angles of attacks. The pressure seems to be constant over the after-body, indicating a separated flow close to the base. The pressure starts to increase, reaching a peak value of 1.8×10^5 Pa at a 3-degree angle and then begins to decrease in an unsteady manner.

The shell of an inflatable vehicle like the Apollo can be deformed through the flight. It is understood that the dominated convex deformations of the vehicles' shell increase the drag force and lift force. Figure 12 depicts the contour deformation for the Apollo during the simulation at a -30-degree angle of attack and a Mach number of 10. It is found that the shell is considerably deformed due to the aerodynamic force.

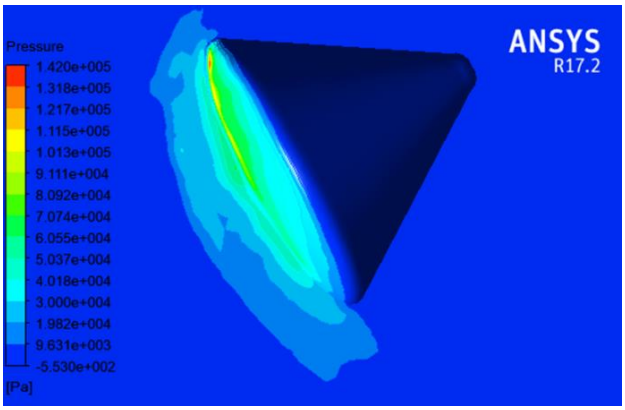

Fig. 10. Variation of pressure contour for Apollo at Mach 10 and AoA =-30°.

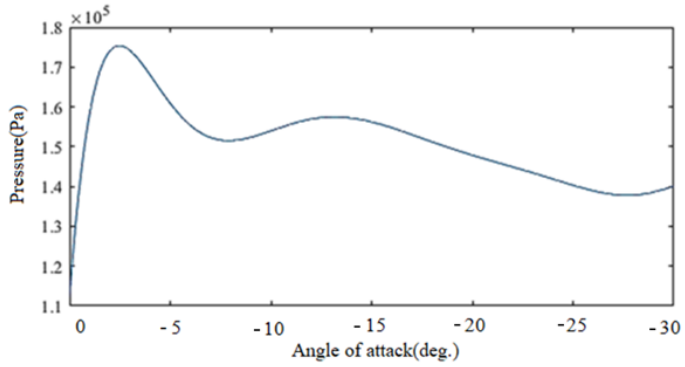

Fig. 11. Pressure distribution at Mach 6 and different values of attack angle.

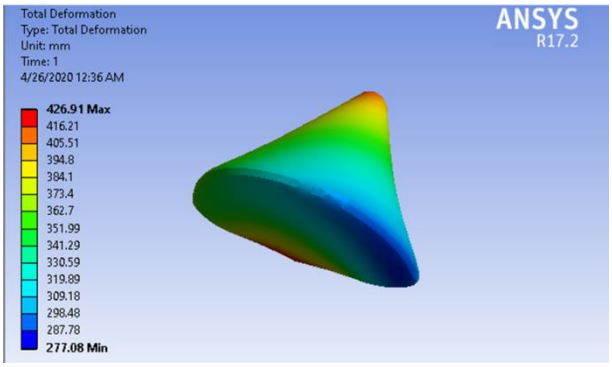

Fig. 12. Variation of deformation contour for Apollo at Mach 10 and AoA =-30°.

Figure 13 displays the vehicle deformation at various angles of attack. It was found that the deformation starts to rise and reaches its peak value at angles of attack between 0 and -5 degrees, and then the deformation starts decreasing. The model of deformation utilized in simulation can likely possess an effect on the prediction of heat flux upon the surface of the shell. The flux of heat upon the shell with the model of deformation gets depressed in comparison with the rigid model. Therefore, it is essential to present a model of shell deformation in the prediction of aerodynamic heating for such a type of vehicle.

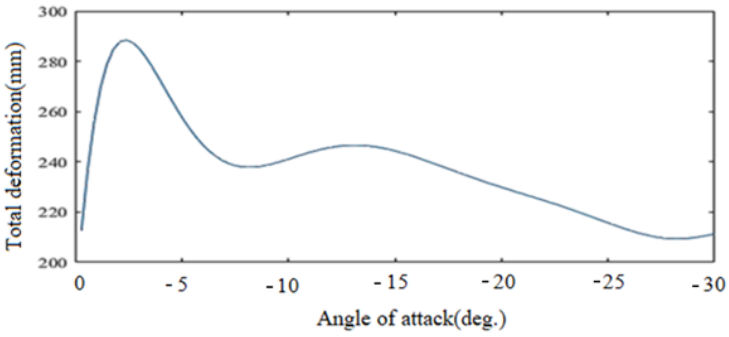

Fig. 13. Total deformation over the Apollo for different values of attack angle at Mach 6.

The equivalent static stress contour and plot with the attack angle are presented in Figs. 14 and 15, respectively. One can observe that the distribution of stress is highly associated with the curve from the existing literature. Also, it is known that the pressure is in direct proportion to the stress impacted on it. Thus, as the pressure is increased, the strain increases at the same rate as the pressure, as seen in Fig. 15. According to these computations, as the Mach number grows, the stagnation pressure increases exponentially to the specific heat ratio. This occurs when the specific heat ratio and the free stream pressure remain constant. The pressure (or stress) acts on the solid object, this object has composite materials, and hence a strain is performed. It could be deduced that the stress is in direct proportion to the exponential model to the Mach number on a re-entry vehicle subjected to higher order Mach numbers. Besides, the strain is in direct proportion to the deformation.

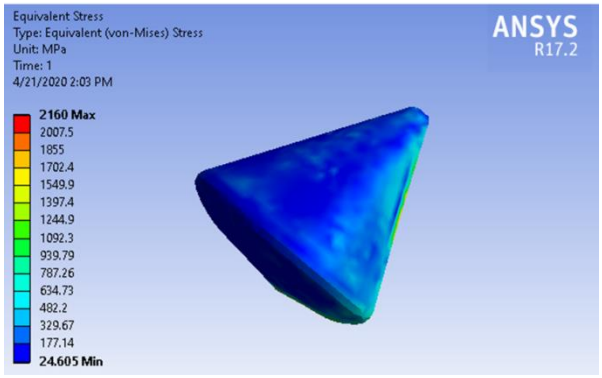

Fig. 14. Variation of stress contour for Apollo at Mach 10 and AoA =-30°.

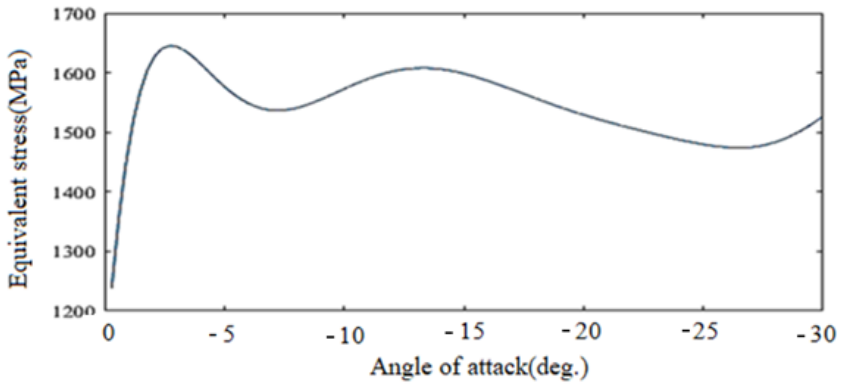

Fig. 15. Stress distribution over the Apollo for different values of attack angle at Mach 6.

5. Conclusions

During the conceptual analysis of a re-entry Apollo, the vehicle shape can be varied, and its impact on performance is evaluated. This work considered a CFD analysis of a 3D capsule entering the atmosphere of Earth. A design analysis was performed to predict the pressure and temperature distribution over the capsule at a variable angle of attack to determine the stress and deformation that occurred on

Apollo. The simulation was carried out using ANSYS finite element program at Mach No. 6 and 10. It was concluded that the potential and kinetic energy were reduced and dissipated in the heat energy form. The extreme temperature was at the fore-body region, and the maximum temperature was at the re-entry vehicle's base. The pressure predicted from CFD methods upon the conical section, in general, agreed with the test of a wind tunnel, and the maximum pressure was found at the forebody. As the pressure increased the deformation, the stress increased at the same growth rate as the pressure. The increase in Mach number increased the stagnation pressure in the exponential form concerning the specific heat ratio. Future opportunities for the improvement of flight apollo are also discussed, especially in regard to areas of technology advancements, cost reduction, and integration with the new Thermal Protection System (TPS).

Acknowledgment

This publication was funded by the Deanship of Scientific Research of Prince Sattam bin Abdulaziz University in Alkharj, Saudi Arabia.

References

1. Curry, D.M. (2019). *Two dimensional analysis of heat and mass transfer in porous media using the strongly implicit procedure*. PhD Thesis, Jobson Space center Houston, Texas.
2. Dirkx, D.; and Mooij, E .(2011). Continues aerodynamic modelling of entry shapes. *Proceedings of AIAA Atmospheric Flight Mechanics Conference*, Netherland, 1-24.
3. Chhunchha, A.C. (2018). *Aerodynamic heating analysis of re-entry space capsule using computational fluid dynamics*. Master Thesis, California State University, USA.
4. Brown, T.G.; Vong, T.; and Topper, B. (2007). Calculating aerodynamic coefficients for a NASA apollo body using telemetry data from free flight range testing. *Proceedings of International Telemetering Conference*, 43, 1-11.
5. Shfeeque, A.P. (2017). CFD Analysis on an atmospheric re-entry module. *International Research Journal of Engineering and Technology*, 4(1), 587-594.
6. Yousefi, M.; Wachiuri, C.; Plaitharathna, V.; Hamdy, M.; Tlili, B.; Barbosu, M.; and Samad, W.A. (2019). Computational design of a CubeSat compatible re-entry capsule. *Proceedings of the 8th European Conference for Aeronautics and Space Sciences (EUCASS)*, Spain, Madrid, 2-15.
7. Jaremkiewicz, M.; Taler, D.; Dzierwa, P.; and Taler, J. (2019). Determination of transient fluid temperature and thermal stresses in pressure thick-walled elements using a new design thermometer. *Energies*, 12(2), 222, 1-21.
8. Giorgio, S.D.; Quagliarella, D; Pezzella, G.; and Pirozzoli, S. (2019). An aerothermodynamics design optimization framework for hypersonic vehicles. *Aerospace Science and Technology*, 84, 339-347.
9. Mehta, R.C. (2018). Numerical simulation of base pressure and drag of space reentry capsules at high speed. *Hypersonic Vehicles - Past, Present and Future Developments*, IntechOpen.

10. Raj, C.A.S.; Narasimhavaradhan, M.; Vaishnavi, N.; Arunvinthan, S.; Arjani, A.A.; and Pillai, S.N. (2020). Aerodynamics of ducted re-entry vehicles. *Chinese Journal of Aeronautics*, 33(7), 1837-1849.
11. Koike, T.; Takahashi, Y.; Oshima, N.; and Yamada, K. (2018). Aerodynamic heating prediction of flare-type membrane inflatable reentry vehicle from low earth orbit. *Proceedings of the 2018 AIAA Atmospheric Flight Mechanics Conference*, 1-21.
12. Hussein, E.Q.; Rashid, F.L.; and Azziz, H.N. (2019). Aerodynamic heating distribution for temperature prediction of fast flying body nose using CFD. *Journal of Advanced Research in Fluid Mechanics and Thermal Sciences*, 64(2), 183-195.
13. Hussein, E.Q.; Azziz, H.N.; and Rashid, F.L. (2021). Aerodynamic study of slotted flap for NACA 24012 airfoil by dynamic mesh techniques and visualization flow. *Journal of Thermal Engineering*, 7(2), 230-239.
14. Wang, H.; and Elgohary, T.A. (2020). A simple and accurate Apollo-trained neural network controller for mars atmospheric entry. *International Journal of Aerospace Engineering*, Volume 2020, Article ID 3793740, 1-15.
15. Schouler, M.; Prévereaud, Y.; and Mieussens, L. (2020). Survey of flight and numerical data of hypersonic rarefied flows encountered in earth orbit and atmospheric reentry. *Progress in Aerospace Sciences*, 118, 100638.
16. de Wit, A.J.; Lammen, W.F.; Vankan, W.J.; Timmermans, H.; van der Laan, T.; and Ciampa, P.D. (2020). Aircraft rudder optimization - A multi-level and knowledge-enabled approach. *Progress in Aerospace Sciences*, 119, 100650.
17. Khanna, A.; and Kotousov, A. (2020). The potential for structural simulation to augment full scale fatigue testing: A review. *Progress in Aerospace Sciences*, 121, 100641.
18. Wright, M.J.; Prabhu, D.K.; and Martinez, E.R. (2006). Analysis of Apollo command module afterbody heating Part I: AS-202. *Journal of Thermophysics and Heat Transfer*, 20(1), 16-30.
19. Rahman, M.H.; Aljibory, M.W.; Rashid, F.L.; and Hussein, E.Q. (2022). Sweep angles influence on the aerodynamic characteristics of NACA 2412 wing with supersonic flow. *Mathematical Modelling of Engineering Problems*, 9(3), 757-761.
20. Weiland, C. (2014). *Aerodynamic data of space vehicles*. *Structural and Competent Collection of Aerothermodynamic*. Springer Berlin, Heidelberg.
21. Thomes, H.; and Harris, S. (2022). New results from Apollo program science. *Proceedings of the 2022 GSA Northeastern Section Mtg. Lancaster, PA, North American*, 15 pages.